Research Square

Preprints are preliminary reports that have not undergone peer review.
They should not be considered conclusive, used to inform clinical practice,
or referenced by the media as validated information.

Spatial and Severity-Dependent Controls of Thermal Comfort Across Türkiye: A SHAP-Based Decomposition of UTCI Drivers

Doğukan Doğu Yavaşlı

dogukan.yavasli@ahievran.edu.tr

Ahi Evran University

Research Article

Keywords: Thermal comfort, UTCI, Explainable AI, SHAP, Random Forest, Eastern Mediterranean, Climate change, Heat stress, Türkiye

Posted Date: May 20th, 2026

DOI: https://doi.org/10.21203/rs.3.rs-9349015/v1

License: This work is licensed under a Creative Commons Attribution 4.0 International License.
Read Full License

Additional Declarations: No competing interests reported.

Version of Record: A version of this preprint was published at Theoretical and Applied Climatology on July 10th, 2026. See the published version at https://doi.org/10.1007/s00704-026-06389-3.

Spatial and Severity-Dependent Controls of Thermal Comfort Across Türkiye: A SHAP-Based Decomposition of UTCI Drivers

Doğukan Doğu Yavaşlı

Department of Geography, Kırşehir Ahi Evran University, Kırşehir, Türkiye

ORCID no: 0000-0002-0150-867X

dogukan.yavasli@ahievran.edu.tr

Abstract

Outdoor thermal stress is intensifying rapidly across Türkiye, yet the meteorological mechanisms driving this intensification remain poorly resolved across the country's contrasting climate regimes. We use a high-resolution explainable artificial intelligence (XAI) framework to quantify the spatially and severity-dependent drivers of outdoor thermal stress across Türkiye. Using ERA5 and ERA5-HEAT reanalysis for 1950-2025 at 0.25° × 0.25° resolution, we assembled 826,799 warm-season grid-day observations under heat-stress conditions (Universal Thermal Climate Index, UTCI > 26 °C). Seven predictors were used in a Random Forest model: 2-m air temperature (T2M), relative humidity (RH), vapor pressure deficit (VPD), wind speed, surface solar radiation downwards (SSRD), surface thermal radiation downwards (STRD), and specific humidity (Q). The global model achieved R^2 = 0.936 and RMSE = 1.80 °C; regional models yielded R^2 values from 0.882 (Black Sea) to 0.964 (Southeastern Anatolia). SHapley Additive exPlanations (SHAP) analysis was applied at global, regional, severity-stratified, and pixel-wise scales. T2M remained the dominant predictor across all UTCI classes, but the relative importance of VPD and STRD increased markedly from moderate (26-32 °C) to very strong heat stress (38-46 °C), whereas wind speed importance declined sharply. Pixel-wise SHAP mapping revealed a clear spatial structure: VPD dominated much of the semi-arid interior, wind speed was more influential along the Black Sea and Marmara coasts, and STRD was most important in parts of the Mediterranean littoral. Very strong and extreme heat grid-days increased by approximately +4.5 and +0.8 grid-days $year^{-1}$, respectively. The results show that thermal stress drivers in Türkiye are neither spatially uniform nor severity-invariant, and that they provide a process-aware basis for regionally differentiated heat-risk adaptation.

Keywords: Thermal comfort; UTCI; Explainable AI; SHAP; Random Forest; Eastern Mediterranean; Climate change; Heat stress; Türkiye

1. Introduction

The Eastern Mediterranean and Middle East (EMME) region has been consistently recognized as a significant global climate change hotspot, demonstrating warming rates that significantly surpass the global mean (Giorgi, 2006; Lelieveld et al., 2012, 2016; Zittis et al., 2022a). Since Giorgi (2006) first identified the Mediterranean as a climate hotspot, later studies have shown that warming in the region is about 20% faster than the global average, with the biggest increases happening in the summer over land surfaces (Lionello and Scarascia, 2018; Cos et al., 2022). In this rapidly warming area, extreme heat events have become much more common, intense, and widespread. Since the 1960s, the number, intensity, and duration of heat waves in the eastern Mediterranean have all increased by six to eight times (Kuglitsch et al., 2010). Projections for high-emission scenarios suggest that summer temperatures will rise by 3.5–7 °C by the end of the century (Lelieveld et al., 2012; Zittis et al., 2016). These changes present significant and cumulative risks to public health, workforce productivity, urban habitability, and ecosystem resilience (Mora et al., 2017; Raymond et al., 2020; Ahmadalipour and Moradkhani, 2018).

The physiological consequences of prolonged heat exposure, which can lead to heat exhaustion, cardiovascular strain, and even death from heatstroke, are not caused by air temperature alone. Instead, they are caused by a complicated mix of weather factors, such as humidity, wind speed, and radiation (Parsons, 2007; Fiala et al., 2012). Sherwood and Huber (2010) showed theoretically that atmospheric moisture is very important for determining the upper limits of human thermoregulatory capacity by setting a wet-bulb temperature limit of 35 °C for human survivability. Vecellio et al. (2022) showed empirically that actual critical Tw thresholds are much lower, around 30.6 °C in humid environments and 25–28 °C in hot-dry conditions. Recent research by Vecellio et al. (2023) integrated empirically established thresholds with CMIP6 projections, indicating a significantly increased global risk from both humid and dry heat stress. The relative significance of specific meteorological variables in influencing thermal stress fluctuates with the intensity of heat exposure and the existing atmospheric conditions. This complexity necessitates analytical methods that can accommodate non-linear, interactive, and spatially diverse relationships among climate drivers.

The Universal Thermal Climate Index (UTCI) has emerged as the most physiologically robust metric for assessing outdoor thermal comfort, integrating the thermodynamic effects of air temperature, mean radiant temperature, wind speed, and humidity through an advanced multi-

node human thermoregulation model (Jendritzky et al., 2012; Fiala et al., 2012; Bröde et al., 2012). Unlike simpler indices such as the Heat Index or Wet Bulb Globe Temperature (WBGT), the UTCI captures the full spectrum of human thermal stress from extreme cold to extreme heat through an adaptive clothing model and multi-segment physiological simulation (Havenith et al., 2012; Błażejczyk et al., 2012). Comparative evaluations have demonstrated UTCI's superior sensitivity to wind speed relative to other indices such as PET (Provençal et al., 2016) and its higher discriminative power for identifying hazardous thermal conditions (Błażejczyk et al., 2012). Since its development within COST Action 730 (Błażejczyk et al., 2013), UTCI has been applied across diverse bioclimatological domains spanning urban climate assessment, tourism climatology, epidemiology, and climate change impact evaluation (Błażejczyk and Kuchcik, 2021; Potchter et al., 2018).

The ERA5-HEAT dataset, developed by the Copernicus Climate Change Service, provides the first global gridded UTCI estimates derived from ERA5 reanalysis at 0.25° × 0.25° spatial resolution and hourly temporal resolution, enabling long-term, spatially continuous thermal comfort assessments at unprecedented scale (Di Napoli et al., 2021). ERA5-HEAT UTCI has been validated against European mortality data across 21 cities (Urban et al., 2021), applied to assess spatiotemporal UTCI changes across the Middle East and North Africa (Hamed et al., 2023), and used in operational thermal health hazard forecasting (Pappenberger et al., 2015). For the EMME region, Di Napoli et al. (2018) identified two distinct European bioclimatic zones using 38 years of reanalysis-based UTCI: a heat-stress-dominated southern and Mediterranean zone and a neutral-to-cold northern zone. Within Türkiye specifically, thermal comfort studies have primarily focused on urban-scale analyses (Yılmaz et al., 2024), while comprehensive national-scale UTCI assessments leveraging the full temporal depth of ERA5-HEAT remain limited.

Even though there are more UTCI datasets and studies, most thermal comfort studies still use traditional statistical methods like correlation analyses, regression models, or index-based trend classifications. These methods don't work well for climate drivers that have nonlinear, interactive, and threshold-dependent relationships (Nazarian et al., 2022; Potchter et al., 2018). The assumption that heat stress is driven uniformly by temperature across all regions and severity levels represents a critical oversimplification. In reality, the transition from moderate to extreme heat stress may be governed by fundamentally different atmospheric mechanisms depending on local topography, maritime influence, and land-surface characteristics. Identifying these spatially and severity-dependent transitions requires

analytical frameworks capable of decomposing complex, high-dimensional interactions without imposing a priori parametric assumptions.

Machine learning (ML) methods, particularly ensemble tree-based models such as Random Forests (Breiman, 2001), have demonstrated exceptional predictive performance in environmental and climate sciences owing to their capacity to model nonlinear relationships and high-order feature interactions (Reichstein et al., 2019). In the thermal comfort domain, ML approaches have been applied for outdoor thermal perception prediction (Guo et al., 2024; Kim et al., 2018) and high-resolution UTCI downscaling (Briegel et al., 2024), consistently outperforming traditional regression methods. The intrinsic opacity of machine learning models, often referred to as the "black-box" problem, has traditionally limited their applicability in scientific contexts that necessitate mechanistic comprehension. The advent of Explainable Artificial Intelligence (XAI) techniques, most notably SHapley Additive exPlanations (SHAP; Lundberg and Lee, 2017), has transformed this landscape by providing theoretically grounded, model-agnostic explanations of individual predictions. SHAP values, rooted in cooperative game theory, quantify the marginal contribution of each input feature to a given prediction, enabling researchers to decompose model outputs into interpretable, additive feature attributions. The TreeExplainer algorithm (Lundberg et al., 2020) enables exact, computationally efficient SHAP value computation for tree-based ensembles. Recent methodological evaluations have confirmed SHAP as a robust and faithful XAI method for climate science applications (Bommer et al., 2024; Flora et al., 2024), while Jiang et al. (2024) have demonstrated how interpretable ML can advance process understanding in the geosciences through spatial SHAP analysis.

A growing number of studies have applied SHAP and related XAI methods to environmental phenomena, including precipitation estimation (He et al., 2023), urban heat island analysis (Hong et al., 2025), and environmental hazard mapping (Wang et al., 2024; Gholami et al., 2024). In the specific domain of outdoor thermal comfort, Guo et al. (2024) used SHAP to reveal that the dominant UTCI driver shifts between mean radiant temperature (in unshaded spaces) and air temperature (in shaded spaces), demonstrating condition-dependent driver hierarchies. However, no study has yet applied XAI to systematically decompose how UTCI driver importance shifts across thermal stress severity categories at the regional climatological scale, a gap that limits both scientific understanding and the design of severity-specific heat mitigation strategies.

The geographic variety of thermal comfort drivers may be studied in an excellent natural laboratory in Turkey, which is located at the crossroads of three main climatic zones:

Mediterranean, continental, and oceanic. The country's seven official geographical regions span humid Black Sea coasts with persistent cloud cover and moderate temperatures, semi-arid Central and Eastern Anatolian plateaus characterized by extreme continental temperature amplitudes and atmospheric desiccation, and the thermally intense Mediterranean and Aegean coastlines where radiative forcing and maritime moisture interact in complex ways (Özturk et al., 2015). This climatic diversity, compressed within a single national territory, provides an opportunity to systematically evaluate how the dominant mechanisms of heat stress shift across contrasting environments.

This study addresses the following research objectives: First, we apply SHAP analysis not only at global and regional aggregates but at the individual 0.25° × 0.25° grid-cell level, producing a pixel-wise map of dominant secondary climate drivers for thermal comfort across the entirety of Türkiye. Second, by independently analyzing four UTCI severity bands (moderate, strong, very strong, and extreme heat stress), we examine how climate driver importance restructures as heat stress intensifies, revealing nonlinear transitions in moisture-related and radiation-related drivers that are invisible to analyses aggregating across severity levels. Third, the extended analysis period (1950-2025) enables assessment of long-term trends in severe heat event frequency, providing temporal context for the observed spatial driver patterns. Because UTCI is itself a meteorologically derived thermal index, our aim is not to treat the machine-learning model as a purely independent predictive exercise, but rather to use it as an interpretable framework for decomposing the relative contributions of related climate drivers across space and heat-stress severity levels.

The primary research question guiding this study is: at severe heat stress thresholds (UTCI > 38 °C), how does the relative importance of individual climate drivers, particularly humidity, wind speed, and radiation, change compared to moderate stress conditions, and do the dominant secondary drivers exhibit systematic spatial patterns corresponding to known climatological gradients? In this context, “importance” refers to model-attributed contribution within an explainable machine-learning framework rather than to independent causal effect size in a strict physical sense.

2. Materials and Methods

2.1. Study Area

The study focuses on Türkiye, a transcontinental country situated predominantly in the Anatolian Peninsula of southwestern Asia, with a smaller portion (Eastern Thrace) extending into southeastern Europe (Figure 1). Türkiye is strategically located within the Eastern Mediterranean basin (approximately 26°E-45°E, 36°N-42°N), a region that has been consistently identified as one of the most prominent climate change hotspots globally, with observed warming rates approximately 20% above the global mean (Lionello and Scarascia, 2018; Zittis et al., 2022a).

Türkiye exhibits extraordinary topographical and climatological complexity within its approximately 783,562 km² territory. Elevations range from sea level along the extensive coastlines to over 5,000 m at Mount Ağrı (Ararat) in the east. This topographic heterogeneity generates a mosaic of distinct climate regimes:

The Black Sea Region is characterized by a humid oceanic climate (Köppen Cfb/Cfa) with persistent cloud cover, year-round precipitation, and moderate temperature amplitudes; the Pontic Mountains create an orographic barrier isolating this region from the continental interior. The Marmara Region exhibits a transitional climate between Mediterranean and oceanic influences, moderated by the Sea of Marmara and the proximity to both the Black Sea and the Aegean. The Aegean Region has a Mediterranean climate (Köppen Csa) with hot, dry summers and mild, wet winters, characterized by strong land-sea breeze circulation patterns and significant insolation during the warm season. The Mediterranean Region displays a hot-summer Mediterranean climate (Köppen Csa) with the highest summer temperatures among coastal regions; the Taurus Mountains create a sharp climate gradient between the coastal strip and the interior plateau. Central Anatolia is dominated by a semi-arid continental steppe climate (Köppen BSk) with extreme temperature amplitudes, low humidity, and limited precipitation across the extensive plateau (average elevation approximately 1,000 m). Eastern Anatolia experiences a severe continental climate with cold winters and warm summers, influenced by high elevation (average approximately 1,500-2,000 m), significant diurnal temperature ranges, and very low atmospheric moisture content. Southeastern Anatolia has a semi-arid to arid climate (Köppen BSh/BWh) with the highest maximum temperatures in Türkiye, frequently exceeding 45 °C during summer, and is characterized by extreme atmospheric desiccation and intense solar radiation.

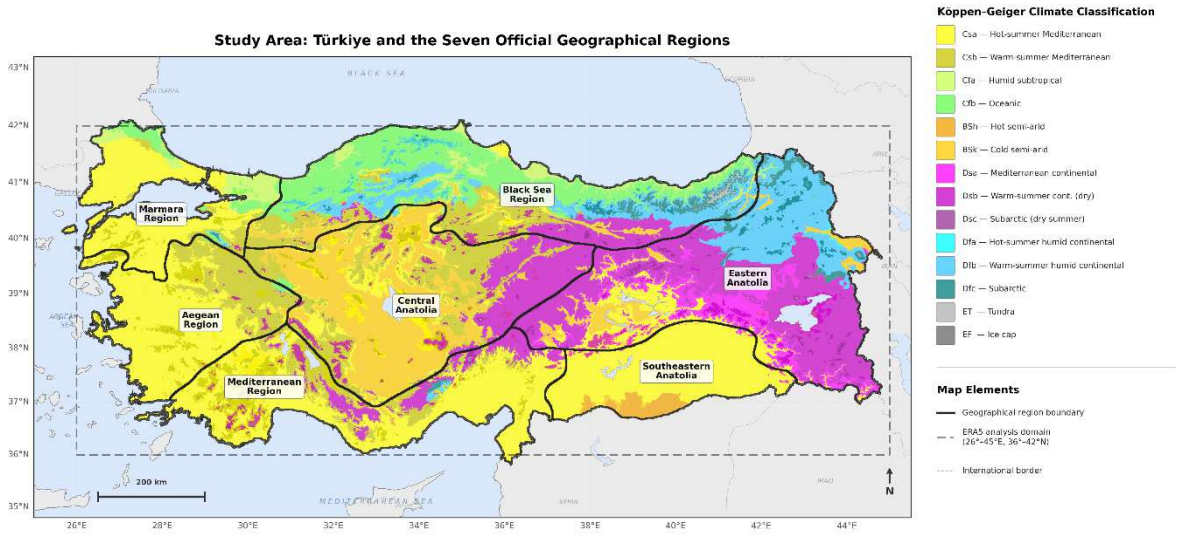


Figure 1. Study area map of Türkiye and its seven official geographical regions. The Köppen–Geiger climate classification background is reproduced from Taşoğlu et al. (2024), with additional overlays showing the official regional boundaries and the ERA5 analysis domain (26°–45°E, 36°–42°N).

To capture this spatial heterogeneity with maximum precision, Türkiye was partitioned into seven official geographical regions following the classification established by the First Turkish Geography Congress of 1941 and maintained by the Turkish Statistical Institute. A ray-casting point-in-polygon algorithm was implemented to allocate each 0.25° × 0.25° grid point to its precise geographic region, preventing the boundary-bleeding artifacts inherent in bounding-box approaches where grid cells near irregular boundaries may be misclassified (see Section 3.6.3 for quantitative validation).

2.2. Climate and Thermal Stress Data

Long-term historical climate data spanning 75 years (1950-2025) were acquired from two complementary European Centre for Medium-Range Weather Forecasts (ECMWF) reanalysis products. The target variable for thermal comfort evaluation, the Universal Thermal Climate Index (UTCI), was obtained from the ERA5-HEAT (Human thErmAl comforT) reanalysis dataset (Di Napoli et al., 2021), available through the Copernicus Climate Data Store (CDS). ERA5-HEAT provides hourly global UTCI estimates at 0.25° × 0.25° spatial resolution, computed from ERA5 atmospheric fields using the UTCI operational procedure (Bröde et al.,

2012). UTCI values represent the equivalent ambient temperature of a reference environment that would elicit the same physiological response as the actual environment, accounting for air temperature, mean radiant temperature, wind speed, and humidity. For each grid point, the daily maximum UTCI was calculated from the hourly values to capture peak thermal stress conditions.

Seven fundamental climate predictor variables were extracted from the ERA5-Land reanalysis (Hersbach et al., 2020; Soci et al., 2024) at its native 0.1° × 0.1° spatial resolution and subsequently regridded to the ERA5-HEAT 0.25° × 0.25° grid using nearest-neighbor interpolation. The predictor variables and their derivations are detailed in Table 1.

Table 1. Climate predictor variables used in the machine learning framework.

Variable	**Abbreviation**	**Unit**	**Source**	**Temporal Aggregation**
2-meter Air Temperature	T2M	°C	ERA5-Land (t2m)	Daily maximum
Relative Humidity	RH	%	Derived from T2M and D2M	Daily mean
Vapor Pressure Deficit	VPD	kPa	Derived from T2M and D2M	Daily mean
Wind Speed	Wind	m/s	Derived from U10 and V10	Daily mean
Surface Solar Radiation Downwards	SSRD	MJ/m²	ERA5-Land (ssrd)	Daily sum
Surface Thermal Radiation Downwards	STRD	MJ/m²	ERA5-Land (strd)	Daily sum

Variable	Abbreviation	Unit	Source	Temporal Aggregation
Specific Humidity	Q	g/kg	Derived from D2M and surface pressure	Daily mean

Relative Humidity (RH) was computed from the 2-meter air temperature (T2M) and 2-meter dew point temperature (D2M) using the Magnus-Tetens approximation:

$$e_s = 6.112 \times \exp\left(\frac{17.67 \times T_{2m}}{T_{2m} + 243.5}\right)$$

$$e_a = 6.112 \times \exp\left(\frac{17.67 \times T_d}{T_d + 243.5}\right)$$

$$RH = 100 \times \frac{e_a}{e_s}$$

where e_s is the saturation vapor pressure (hPa) and e_a is the actual vapor pressure (hPa).

Vapor Pressure Deficit (VPD), representing the atmospheric moisture demand and a critical determinant of human evaporative cooling capacity, was calculated as:

$$VPD = \frac{e_s - e_a}{10} \text{[kPa]}$$

using saturation and actual vapor pressures derived via the Magnus formula:

$$e_s = 0.6108 \times \exp\left(\frac{17.27 \times T_{2m}}{T_{2m} + 237.3}\right)$$

$$e_a = 0.6108 \times \exp\left(\frac{17.27 \times T_d}{T_d + 237.3}\right)$$

Saturation and actual vapour pressure were computed using the FAO Penman-Monteith form of the Magnus equation (Allen et al., 1998), applied consistently for all derived humidity variables (RH, VPD, and q).

Wind Speed was computed as the resultant of the 10-meter eastward (U10) and northward (V10) wind components:

$$\text{Wind} = \sqrt{U_{10}^2 + V_{10}^2}$$

The temporal domain was restricted to the extended warm season (April-October) to focus on heat stress conditions, as thermal discomfort from heat in the study region is negligible during the November-March period.

2.3. Data Preprocessing and Stratification

The preprocessing pipeline consisted of five sequential stages. First, data were restricted to the extended warm season months (April through October, inclusive) to isolate the period relevant for heat stress assessment. Second, ERA5-Land variables at 0.1° × 0.1° resolution were regridded to the ERA5-HEAT 0.25° × 0.25° grid using nearest-neighbor interpolation to ensure spatial consistency between predictor and target variables. Third, for each 0.25° × 0.25° grid cell, hourly UTCI values were aggregated to daily maximum UTCI (representing peak thermal stress), while predictor variables were aggregated as daily maxima (T2M), daily means (RH, VPD, Wind, Q), or daily sums converted to MJ/m² (SSRD, STRD). Fourth, to strictly analyze heat stress mechanisms rather than general thermal conditions, the dataset was filtered to retain only grid-day observations where the daily maximum UTCI exceeded 26.0 °C, corresponding to the onset of "moderate heat stress" as defined by the UTCI assessment scale (Bröde et al., 2012); this threshold-based filtering ensures that the machine learning model and subsequent SHAP analysis are trained exclusively on physiologically relevant heat stress conditions. Fifth, the continuous UTCI values were classified into four established heat stress severity bands following the standard UTCI assessment scale: moderate heat stress (26-32 °C), strong heat stress (32-38 °C), very strong heat stress (38-46 °C), and extreme heat stress (>46 °C). The final preprocessed dataset comprised 826,799 grid-day observations across the 75-year study period, stored as an optimized Apache Parquet feature matrix for computational efficiency.

2.4. Machine Learning Framework

2.4.1. Model Selection and Architecture

A Random Forest (RF) Regressor (Breiman, 2001) was selected as the predictive model for several methodologically motivated reasons: (i) RF models handle nonlinear relationships and high-order feature interactions without requiring explicit specification; (ii) they are robust to

multicollinearity among predictors, which is expected given the thermodynamic interdependencies among climate variables; (iii) they provide built-in out-of-bag error estimation; and (iv) the TreeExplainer algorithm enables exact, computationally efficient SHAP value computation for tree-based ensembles (Lundberg et al., 2020). Because the target variable (UTCI) is itself derived from meteorological inputs conceptually related to the predictor set, the RF model is used here primarily as a stable, interpretable decomposition framework rather than as an end in itself for independent prediction.

The RF model was configured with the following hyperparameters, selected through preliminary cross-validation experiments:

Table 2. Random Forest Regressor hyperparameter configuration.

Parameter	**Value**	**Justification**
Number of estimators	500	Sufficient for convergence with diminishing returns beyond this threshold
Maximum depth	12	Balances model complexity against overfitting risk
Minimum samples per leaf	20	Prevents overly specific terminal nodes
Minimum samples per split	40	Ensures statistically meaningful splits
Maximum features per split	sqrt(p)	Standard heuristic for regression forests
Random state	42	Ensures reproducibility

2.4.2. Training Strategy

Three categories of models were independently trained and evaluated. A global model was trained on the entire Türkiye dataset (n = 826,799) to capture country-wide thermal comfort dynamics. Seven regional models were trained on geographically subsetted data, with each grid point allocated to its region using the polygon-based classification described in Section 2.1; regional sample sizes ranged from 59,139 (Marmara) to 161,403 (Central Anatolia). Four

297 severity-stratified models were trained separately on data from each UTCI severity band to
298 evaluate how driver importance shifts with heat stress intensity.

299 For each model, the data were split into training (80%) and testing (20%) sets using stratified
300 random sampling with a fixed random seed (42) for reproducibility. Model performance was
301 evaluated using the Coefficient of Determination (R^2) and Root Mean Square Error (RMSE)
302 computed on the held-out test set.

303 2.5. Explainable AI (XAI) Framework

304 *2.5.1. SHAP Value Computation*

305 To overcome the opacity of the RF model and extract mechanistic insights, SHapley Additive
306 exPlanations (SHAP; Lundberg and Lee, 2017) were integrated at multiple analytical scales.
307 SHAP values are grounded in Shapley values from cooperative game theory, where each
308 feature is treated as a "player" in a coalition, and its contribution to the prediction is computed
309 as the weighted average of its marginal contributions across all possible feature coalitions. For
310 a prediction $f(x)$, the SHAP value ϕ_j for feature j satisfies the additive decomposition:

311 $$f(x) = \phi_0 + \sum_{j=1}^{p} \phi_j\,(x)$$

312 where ϕ_0 is the expected model output (base value) and $\phi_j(x)$ represents the contribution of
313 feature j to the deviation from the base value for instance x.

314 The TreeExplainer algorithm (Lundberg et al., 2020) was used to compute exact SHAP values
315 in polynomial time for tree-based models. Feature importance was quantified as the mean
316 absolute SHAP value ($|\bar{\phi}_j|$) across all instances, representing the average magnitude of each
317 feature's contribution to the predicted UTCI, expressed in degrees Celsius. These attributions
318 should be interpreted as model-based contribution magnitudes within the fitted predictor
319 space, not as direct estimates of independent physical effect size.

320 *2.5.2. Multi-Scale SHAP Analysis*

321 SHAP analysis was conducted at four complementary scales. At the global scale, SHAP
322 summary plots (beeswarm plots) for the Whole Türkiye model were generated, revealing
323 overall feature importance and the direction of feature effects. At the regional scale,
324 independent SHAP analyses for each of the seven geographic regions identified the top three
325 climate drivers per region and their relative rankings. At the severity-stratified scale, SHAP

importance matrices were computed separately for each UTCI severity band and visualized as heatmaps to reveal how driver importance shifts with intensifying heat stress. At the pixel-wise scale, for every distinct geographic grid cell in the dataset, the mean climate conditions during heat events were computed and SHAP values were calculated using the global model; the dominant secondary driver (the highest-importance feature excluding T2M) was identified for each pixel, producing a high-resolution 0.25° × 0.25° spatial map of driver dominance across Türkiye.

2.5.3. SHAP Dependence Analysis

SHAP dependence plots were generated for key features (T2M and RH) to examine nonlinear interaction effects. Each dependence plot displays the SHAP value of a feature against its actual value, with points colored by a secondary interacting feature, revealing how the effect of one climate driver on UTCI is modulated by another.

3. Results

3.1. Temporal Trends of Extreme Heat Stress (1950-2025)

The 75-year longitudinal analysis reveals a pronounced intensification of severe heat stress events across Türkiye (Figure 2). The trend analysis focuses on the Very Strong (38–46 °C) and Extreme (>46 °C) UTCI categories because Strong Heat Stress conditions (32–38 °C) are already pervasive across Türkiye's warm season in the earliest decades of the record, limiting the statistical sensitivity of trend detection in this band; the upper tail categories carry the greatest public health significance and exhibit the clearest signal-to-noise characteristics for long-term trend assessment. Annual counts of "Very Strong Heat" (UTCI 38-46 °C) grid-days exhibit a strong upward trend, increasing at approximately **+4.5 grid-days per year** over the study period. Although inter-annual variability is substantial, with annual counts fluctuating between approximately 400 and 1,300 grid-days, the linear trend trajectory demonstrates a clear secular increase. By the most recent decade (2015-2025), very strong heat grid-days regularly exceed 1,000 per year, compared to a baseline of approximately 500-700 during the 1950-1970 period.

"Extreme Heat" (UTCI > 46 °C) grid-days, while less frequent in absolute terms, show a positive linear slope of **+0.8 grid-days per year**, though this trend does not reach conventional statistical significance (Mann-Kendall $\tau = 0.132$, $p = 0.092$). These events were exceedingly rare during the 1950-1970 baseline period (typically 0-50 grid-days per year) but

have become more common since the mid-1990s, with individual years recording 100-350 extreme heat grid-days. In contrast, the very strong heat trend is highly significant (Mann-Kendall $\tau = 0.336$, $p < 0.001$), confirming a robust secular intensification of severe thermal stress. These trends are consistent with broader Eastern Mediterranean warming patterns documented in the IPCC AR6 (Ali et al., 2022), long-term UTCI trend analyses for the MENA region showing increases of 0.1-0.7 °C per decade (Hamed et al., 2023), and regional projections anticipating further intensification of summer heat extremes (Zittis et al., 2016; Ntoumos et al., 2022).

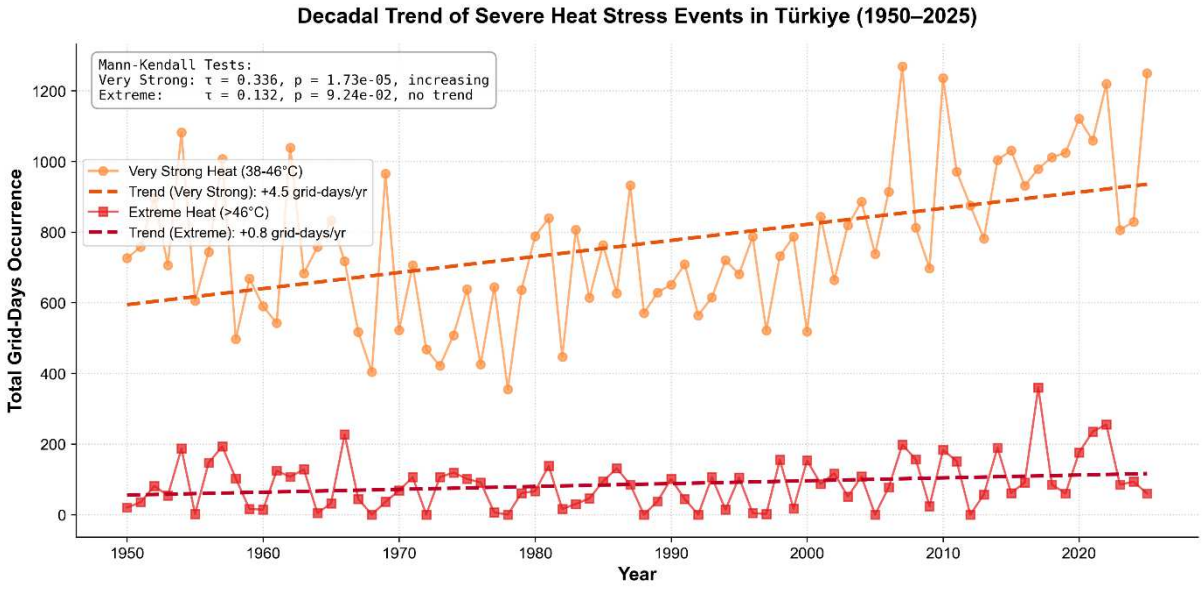


Figure 2. Temporal trend of severe heat stress events in Türkiye (1950-2025). Orange circles and line: annual count of "Very Strong Heat" (UTCI 38-46 °C) grid-days. Red squares and line: annual count of "Extreme Heat" (UTCI > 46 °C) grid-days. Dashed lines indicate linear regression trend trajectories. Mann-Kendall trend tests are annotated: Very Strong Heat shows a statistically significant increasing trend ($\tau = 0.336$, $p < 0.001$), while the Extreme Heat trend is positive but not statistically significant ($\tau = 0.132$, $p = 0.092$).

3.2. Global Model Performance and Validation

The Random Forest model trained on the full Türkiye dataset (n = 826,799) achieved high predictive accuracy, with $R^2 = 0.936$ and RMSE = 1.80 °C on the held-out test set (20% of data; Figure 3). It should be noted that UTCI is itself derived from meteorological variables (temperature, humidity, wind, radiation) that are conceptually related to the predictor set; consequently, high predictive skill is partly structural. The scientific value of the model therefore lies not primarily in predictive performance itself but in the subsequent SHAP

decomposition of feature importance across space and severity classes. Accordingly, model skill is interpreted here as evidence that the fitted framework is sufficiently stable for attribution-focused analysis, rather than as the principal contribution of the study. The observed-versus-predicted density scatter plot reveals tight clustering along the 1:1 diagonal across the UTCI spectrum, from moderate heat stress, with negligible systematic bias.

The hexbin density visualization demonstrates that the highest prediction densities are concentrated in the 26-35 °C range, corresponding to the most frequently observed UTCI conditions in the dataset. Model performance remains robust at the extreme tails of the distribution (UTCI > 40 °C), where accurate predictions are most consequential for public health applications. The slight dispersion at the highest UTCI values (>45 °C) reflects both the inherent stochasticity of extreme events and the smaller sample sizes in this severity band, but the overall predictive envelope remains well-calibrated.

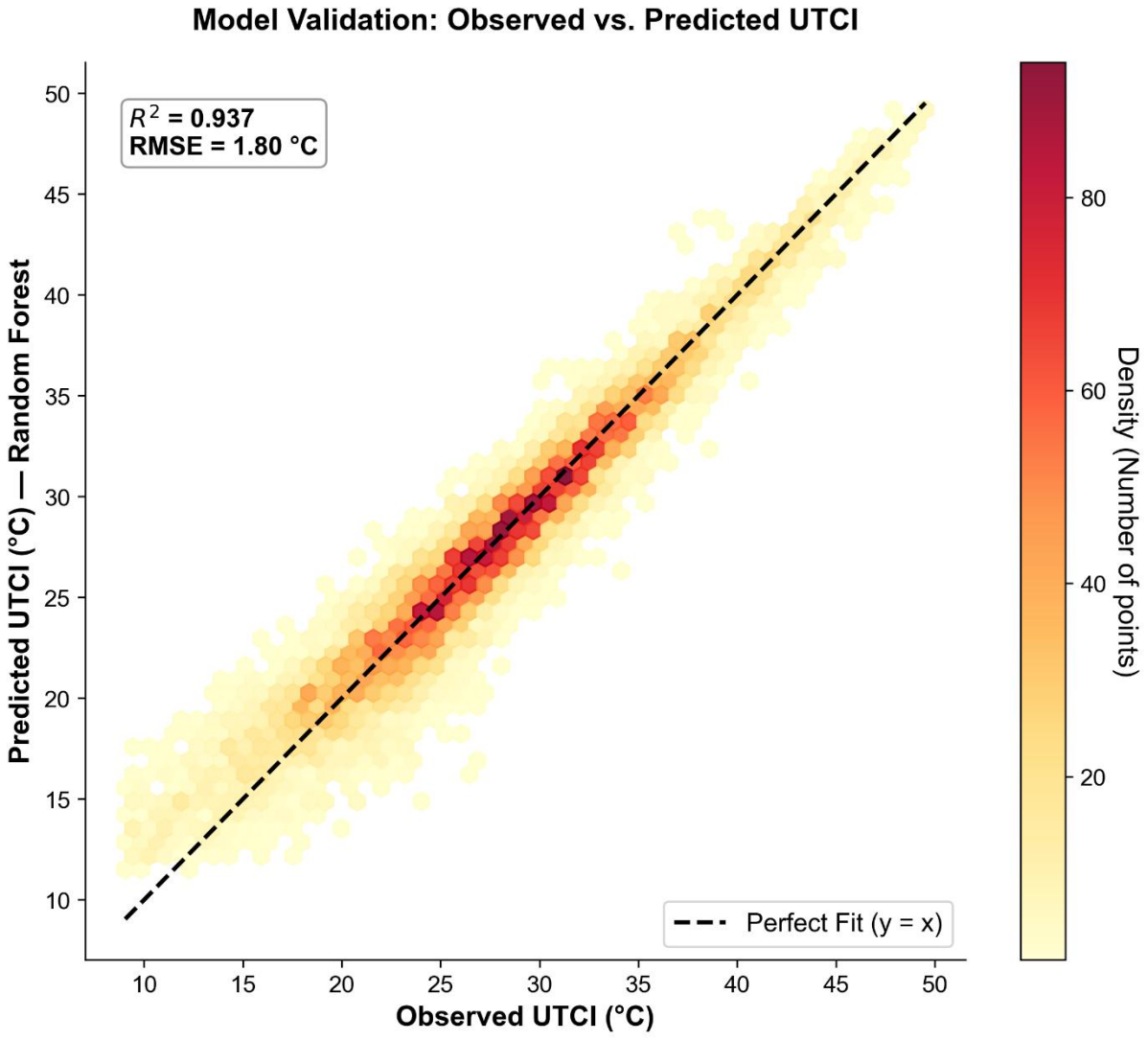


Figure 3. Model validation scatter plot: Observed versus Predicted UTCI for the global (Whole Türkiye) Random Forest model. Color intensity (hexbin density) represents the number of data points in each cell. The dashed black line indicates perfect prediction (y = x). R^2 = 0.936 and RMSE = 1.80 °C on the held-out test set (n ≈ 165,000).

3.3. Regional Model Performance and Driver Rankings

Regional models demonstrated consistently high predictive accuracy across all seven geographic regions, with R^2 values ranging from 0.882 to 0.964 (Figure 4; Table 3). The inter-regional variation in model performance provides meaningful insights into the climatological complexity of each region.

Table 3. Regional model performance metrics and SHAP-derived climate driver rankings.

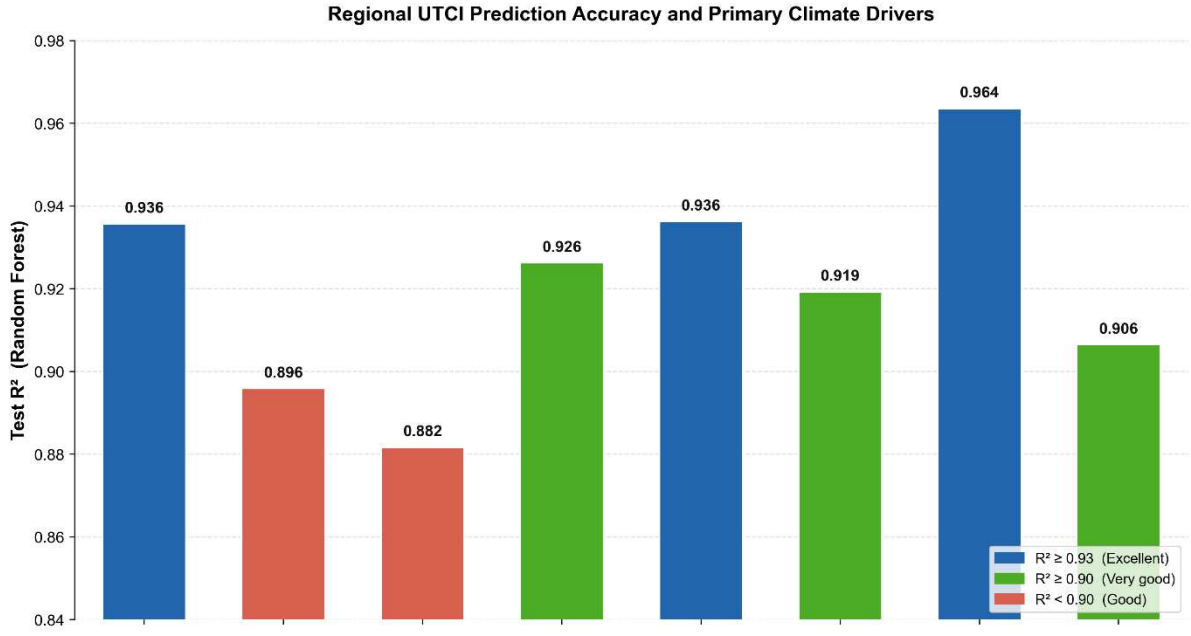
Region	**N Samples**	**R^2**	**1st Driver**	**2nd Driver**	**3rd Driver**
Whole Türkiye	826,799	0.936	T2M	VPD	Wind
Southeastern Anatolia	65,274	0.964	T2M	VPD	RH
Aegean Region	75,527	0.936	T2M	VPD	Wind
Marmara Region	59,139	0.926	T2M	Wind	VPD
Central Anatolia	161,403	0.919	T2M	VPD	Wind
Mediterranean Region	76,708	0.906	T2M	VPD	STRD
Eastern Anatolia	133,709	0.896	T2M	VPD	Wind
Black Sea Region	101,529	0.882	T2M	VPD	Q

Southeastern Anatolia achieved the highest model accuracy ($R^2 = 0.964$), reflecting the region's relatively homogeneous semi-arid climate where thermal dynamics are governed by a consistent set of drivers (T2M, VPD, RH). The limited cloud cover and moisture variability in this region produce highly predictable UTCI responses to the input climate variables.

The Black Sea Region yielded the lowest, yet still robust, model accuracy ($R^2 = 0.882$). This reduced performance is attributable to the region's exceptional climatological complexity: persistent cloud cover creates highly variable radiation conditions, orographic effects modulate wind patterns unpredictably, and the persistent maritime moisture supply generates complex humidity-temperature interactions that challenge even nonlinear models. The emergence of Specific Humidity (Q) as the third-ranked driver which is unique among all regions, reflects the fundamental role of absolute atmospheric moisture content in determining thermal comfort along this persistently humid coastline.

The Marmara Region is the only region where Wind Speed displaces VPD as the second-most-important driver, reflecting the strong influence of the Bosphorus and Dardanelles strait winds, combined with the moderating effects of the Sea of Marmara on the regional thermal environment.

The Mediterranean Region is distinguished by STRD (Thermal Radiation) as the third-ranked driver, consistent with the intense surface heating, clear-sky conditions, and high longwave radiative forcing that characterize the southern Turkish coast during summer.



	Whole Türkiye	Eastern Anatolia	Black Sea Region	Marmara Region	Aegean Region	Central Anatolia	Southeastern Anatolia	Mediterranean Region
1st Driver	T2M	T2M	T2M	T2M	T2M	T2M	T2M	T2M
2nd Driver	VPD	VPD	VPD	Wind	VPD	VPD	VPD	VPD
3rd Driver	Wind	Wind	Q	VPD	Wind	Wind	RH	STRD

Figure 4. Regional UTCI prediction accuracy (R^2) and SHAP-derived primary, secondary, and tertiary climate drivers for each of Türkiye's seven geographical regions. Bar colors indicate performance tiers: blue ($R^2 \geq 0.93$), green ($R^2 \geq 0.90$), and red ($R^2 < 0.90$). The table below the chart lists the top three climate drivers ranked by mean absolute SHAP value for each region.

3.4. Severity-Stratified Driver Importance

The SHAP-derived feature importance matrix, stratified across the four UTCI severity bands, reveals a dynamic and nonlinear restructuring of climate driver importance as heat stress intensifies (Figure 5). These SHAP values quantify model-attributed importance, namely the contribution of each predictor to the fitted Random Forest's predictions, rather than direct physical effect sizes.

Several critical patterns emerge from this severity-stratified decomposition. The three most important drivers (T2M, VPD, and STRD) all exhibit a marked escalation in absolute SHAP contribution as heat stress severity increases from moderate to very strong categories. T2M SHAP values increase by 59% (from 0.574 to 0.913 °C), VPD by 66% (from 0.339 to 0.561 °C), and STRD by 100% (from 0.233 to 0.467 °C) between moderate and very strong heat

stress. This indicates that the physical mechanisms producing extreme thermal discomfort are qualitatively different from those governing moderate conditions, not merely amplified versions of the same dynamics.

In contrast, wind speed, which ranks as the third most important driver during moderate heat stress (mean |SHAP| = 0.313 °C), undergoes a dramatic decline at higher severities, dropping to 0.019 °C during extreme heat events with a 94% reduction. This pattern has a clear thermophysiological interpretation: at moderate heat stress levels, convective and evaporative cooling via wind provides meaningful mitigation; however, under extreme conditions where air temperature exceeds skin temperature (~35 °C), wind accelerates rather than mitigates convective heat transfer to the body, rendering ventilation counterproductive. This finding aligns with the experimental work of Bröde and Kampmann (2023), who demonstrated that wind reduces physiological strain below 35 °C but increases it in hot-dry conditions above this threshold.

The disproportionate increase in VPD and STRD importance at very strong and extreme heat stress levels demonstrates that entry into physiologically dangerous thermal zones is governed predominantly by boundary-layer moisture mechanisms (VPD) and radiative forcing (STRD) rather than by raw temperature increments alone. At very strong heat stress, VPD and STRD combined contribute 1.028 °C of mean absolute SHAP impact, representing 53% of T2M's contribution; a ratio that is only 37% during moderate heat stress.

The apparent reduction in all SHAP values at the extreme heat band (>46 °C) reflects the smaller sample size and the compression of feature variability at these conditions, where all drivers simultaneously assume high values, reducing the marginal discriminative power of any single variable. These shifts should be interpreted as changes in model-attributed driver salience across the UTCI severity spectrum, rather than as direct one-to-one estimates of physiological effect magnitude.

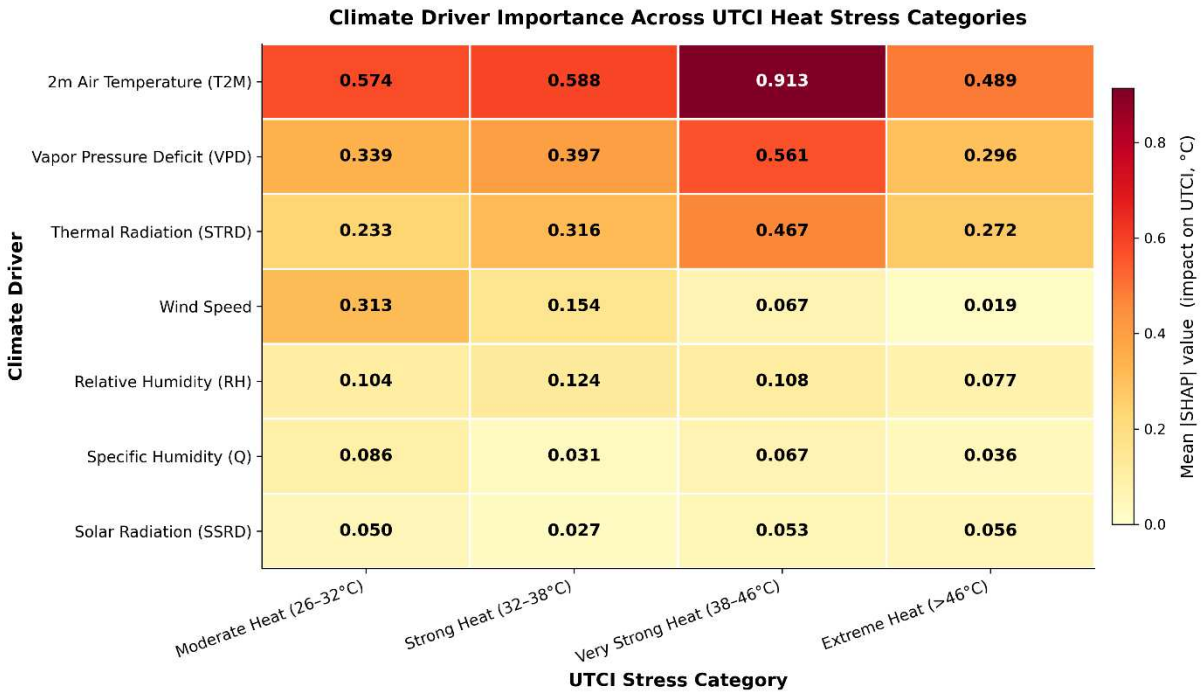


Figure 5. SHAP-derived climate driver importance heatmap across UTCI heat stress severity categories. Cell values represent mean absolute SHAP values (°C). Color intensity scales from light (low importance) to dark red (high importance). Note the progressive intensification of T2M, VPD, and STRD from moderate to very strong heat stress, and the simultaneous collapse of wind speed importance.

3.5. Temperature versus Humidity Dynamics

The relationship between air temperature and humidity contributions to thermal stress was further examined through fine-resolution SHAP analysis across 2 °C UTCI bins (Figure 6). The absolute SHAP contributions of both T2M and RH increase with UTCI intensity, but T2M contributions escalate far more steeply. At the lowest bin (26-30 °C), T2M contributes 1.10 °C while RH contributes 0.55 °C. At the highest bin (46-50 °C), T2M reaches 8.32 °C while RH reaches 2.62 °C.

The RH/T2M SHAP dominance ratio analysis (Figure 6, right panel) reveals that temperature remains consistently dominant over relative humidity across all UTCI bins, with the ratio never exceeding 1.0. The ratio is highest at the lowest UTCI bin (0.50 at 26-30 °C) and decreases to approximately 0.26-0.32 at higher stress levels. The correct conclusion is therefore not humidity dominance, but persistent temperature primacy accompanied by a severity-dependent increase in moisture-related influence. This pattern is consistent with the finding of Simpson et al. (2023), who showed that commonly used thermal indices disagree

about the relative importance of moisture precisely because this importance varies systematically across the intensity spectrum of thermal stress.

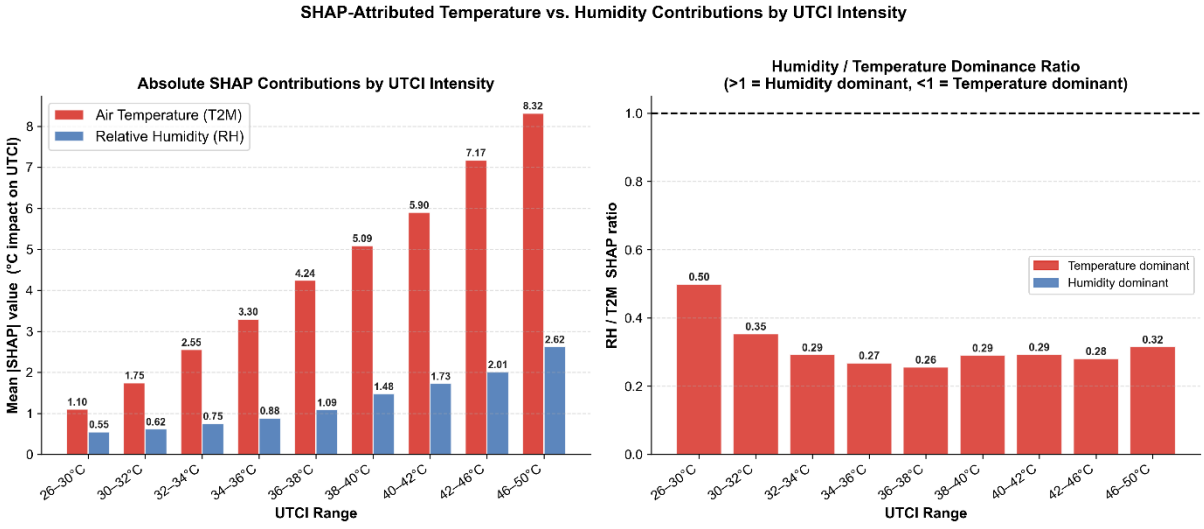


Figure 6. Model-attributed temperature versus humidity SHAP contributions across UTCI heat-stress bands. Left panel: absolute SHAP contributions of T2M (red) and RH (blue) by 2 °C UTCI bins. Right panel: RH/T2M SHAP dominance ratio (values > 1 would indicate humidity dominance). Temperature remains dominant across all severity levels, with the ratio peaking at 0.50 in the 26-30 °C range and declining at higher stress levels.

3.6. High-Resolution Spatial Heterogeneity of Climate Drivers

3.6.1. Regional Choropleth Map

The regional-scale cartographic visualization (Figure 7) provides a synoptic overview of the spatial distribution of tertiary climate drivers across Türkiye's seven geographic regions. With T2M universally ranking as the primary driver and VPD as the secondary driver in six of seven regions, the tertiary driver reveals the most informative spatial differentiation. Central Anatolia, the Aegean, Eastern Anatolia, and Marmara share wind as their tertiary driver, although the processes underpinning this pattern differ, reflecting convective cooling over the arid plateau and sea-breeze influences along the coasts. The Mediterranean coastline is uniquely characterized by thermal radiation (STRD) as its tertiary driver, reflecting intense surface heating, clear-sky longwave emission, and the thermal amplification effect of the Taurus Mountain barrier. Specific humidity (Q) emerges as the tertiary driver only in the Black Sea region, where persistent oceanic moisture supply and orographic precipitation maintain high absolute humidity levels throughout the warm season. In Southeastern Anatolia,

relative humidity (RH) serves as the tertiary driver, reflecting the critical role of even modest moisture fluctuations in modulating extreme heat stress where baseline humidity is very low.

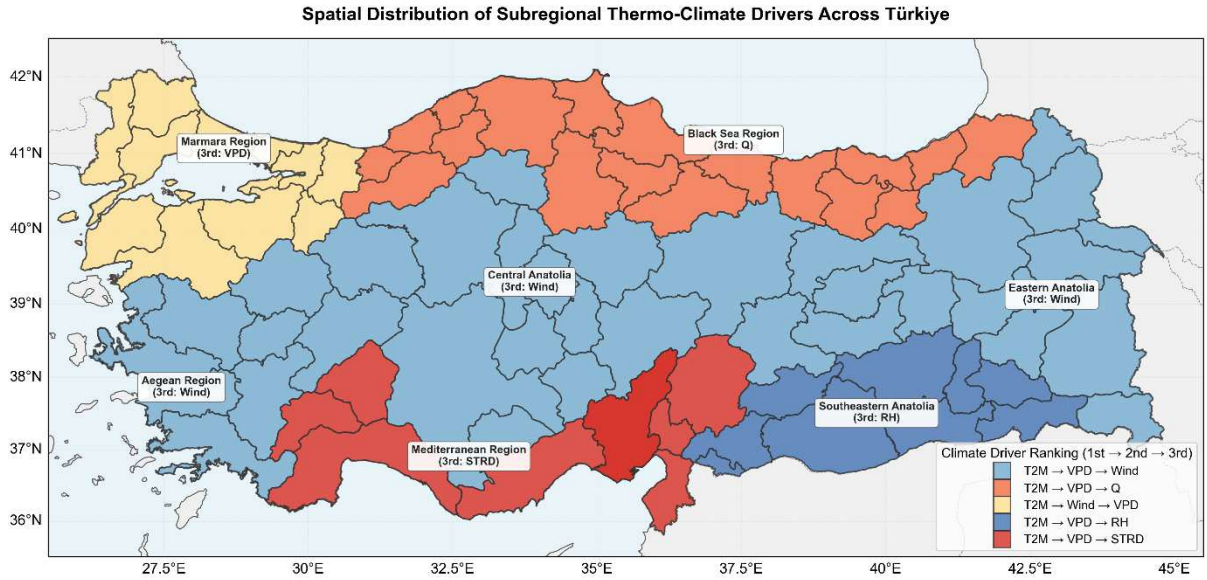


Figure 7. Spatial distribution of subregional thermo-climate driver dominance across Türkiye (TopoJSON polygon boundaries). Regions are colored according to their top three climate driver combinations. T2M and VPD are the first and second drivers in six of seven regions; the tertiary driver captures the most informative regional differentiation.

3.6.2. Pixel-Wise SHAP Dominance Map

The 0.25° × 0.25° pixel-wise map of dominant secondary climate drivers, computed by applying SHAP analysis to the mean climate conditions of every geographic grid cell during heat events (Figure 8), bypasses regional aggregation entirely, revealing intra-regional heterogeneity that is invisible in choropleth representations.

The pixel-wise map exposes three fundamental spatial regimes. The vast semi-arid interiors, spanning Central Anatolia, Eastern Anatolia, Southeastern Anatolia, and the inland portions of the Aegean and Mediterranean regions, show VPD as the dominant secondary driver. This spatial coherence reflects the thermodynamic reality that in arid and semi-arid environments, where air temperatures routinely exceed skin temperature, the atmospheric moisture deficit (VPD) determines the rate of evaporative cooling from the human body. The geographic extent of VPD dominance encompasses approximately 60-65% of Türkiye's land area,

underscoring the pervasive influence of atmospheric desiccation on thermal comfort across the Anatolian landmass.

A distinct band of wind-dominated pixels lines the Black Sea coast and extends westward through the Marmara region. The XAI framework has autonomously identified that in environments where humidity is persistently high and temperature amplitudes are moderate (oceanic climate), sensible heat loss via convective wind cooling becomes the critical mitigating variable. The Pontic Mountains create a sharp transition: pixels immediately inland from the mountain crest shift abruptly from wind to VPD dominance, demonstrating the orographic control on climate driver regimes.

Along the Aegean and Mediterranean coastlines, STRD (thermal radiation) emerges as the dominant secondary driver in discrete pixel clusters. High surface heating from exposed limestone and karst terrain, combined with clear-sky conditions during the summer months, produces intense longwave ground emissions that significantly increase the thermal radiation environment. The patchy spatial distribution of STRD-dominant pixels along the coast reflects the localized nature of radiative forcing, which is modulated by terrain aspect, surface albedo, and proximity to the sea.

Isolated pixels dominated by RH, Q, or SSRD appear in transitional zones and at higher elevations, representing microclimatic niches where specific humidity gradients or solar radiation variability locally override the dominant VPD signal.

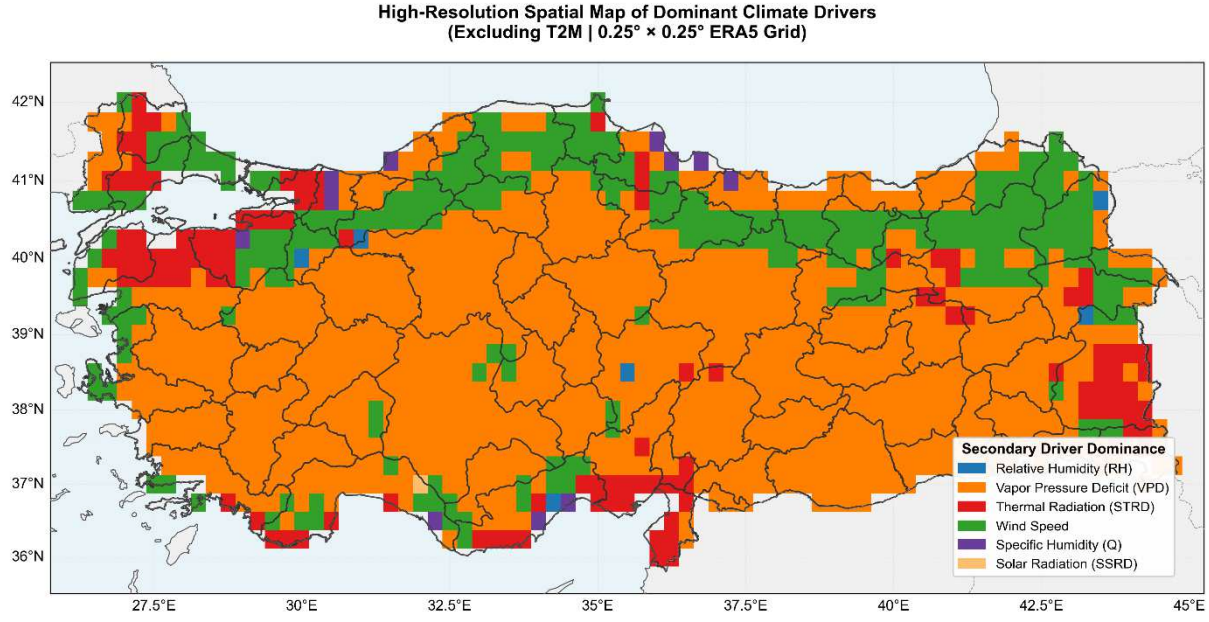


Figure 8. High-resolution (0.25° × 0.25°) spatial map of dominant secondary climate drivers for thermal comfort across Türkiye, excluding T2M. Each pixel is colored by the climate variable with the highest mean absolute SHAP value (after T2M) based on mean heat-event conditions. Orange: VPD; Green: Wind Speed; Red: STRD; Blue: RH; Purple: Q; Yellow: SSRD.

3.6.3 Regional SHAP Summary Analysis

Individual SHAP summary (beeswarm) plots for the national model and seven regional models are presented as a composite panel in Figure 9. T2M dominates in every region, but the secondary and tertiary driver hierarchies diverge in ways that are consistent with the regional climatological characteristics described in Section 2.1.

At the national scale (Figure 9a), VPD ranks second and Wind Speed third, with STRD and RH contributing at lower magnitudes. The Black Sea Region (Figure 9d) presents the most distinctive profile: Specific Humidity (Q) rises to third position, unique among all regions, reflecting the persistent oceanic moisture supply, while wind speed exhibits particularly strong bidirectional effects (up to −4 °C), demonstrating the critical cooling role of maritime ventilation. The relatively compressed SHAP range across all features reflects the temperature-moderating influence of the Black Sea. Southeastern Anatolia (Figure 9g) shows the widest T2M SHAP range (approximately −6 to +8 °C), reflecting the extreme temperature amplitudes of this semi-arid zone; RH appears as the third driver, also unique, indicating that even modest humidity fluctuations in this inherently dry environment significantly modulate thermal comfort, while wind speed clusters near zero, confirming that ventilation plays a negligible role.

The Mediterranean Region (Figure 9h) is distinguished by STRD's elevated importance (third position), consistent with intense longwave radiative forcing from sun-heated limestone terrain. Wind speed shows a bimodal pattern in which high wind values mitigate UTCI while calm conditions amplify it, consistent with the importance of sea breeze circulation for coastal thermal comfort. The Marmara Region (Figure 9b) is the only region where Wind Speed displaces VPD as the second-most-important driver, reflecting the unique influence of the Bosphorus and Dardanelles strait winds and the Sea of Marmara's thermal moderation. Central (Figure 9e) and Eastern Anatolia (Figure 9f) share structurally similar profiles dominated by T2M and VPD, though Eastern Anatolia exhibits a compressed overall SHAP range reflecting altitude-moderated temperature extremes. The Aegean profile (Figure 9c)

closely resembles the national average, with T2M, VPD, and Wind Speed as the top three drivers.

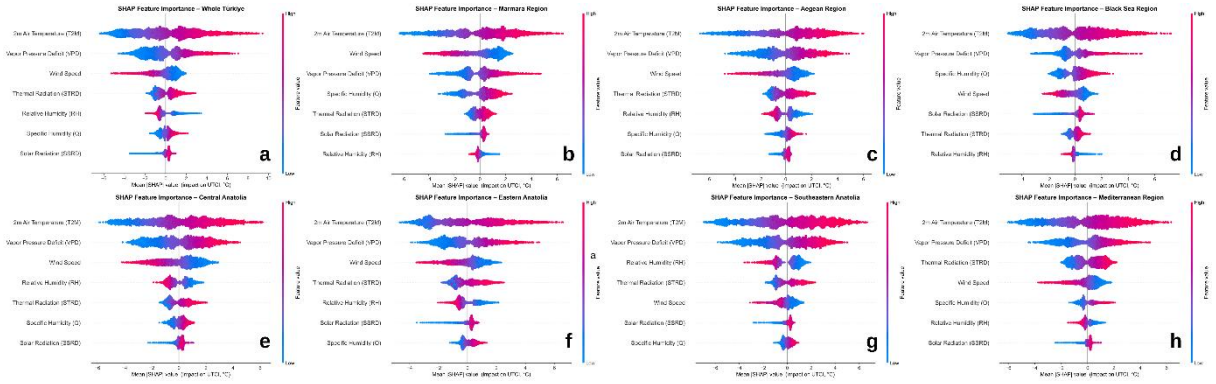


Figure 9. Composite SHAP beeswarm plots for the national model and seven regional models. (a) Whole Türkiye, (b) Marmara Region, (c) Aegean Region, (d) Black Sea Region, (e) Central Anatolia, (f) Eastern Anatolia, (g) Southeastern Anatolia, (h) Mediterranean Region. Each point represents a single prediction; horizontal position indicates the SHAP value (impact on UTCI in °C), and color indicates the feature value (red/pink = high, blue = low). Features are ordered by mean absolute SHAP value within each panel.

3.7. SHAP Dependence Interactions

The SHAP dependence plots for T2M and RH reveal the nature of the temperature-humidity interaction (Figure 10). T2M Dependence (Figure 10a). The T2M SHAP value increases approximately linearly with air temperature, transitioning from strongly negative contributions at low temperatures (~0 °C, SHAP ≈ −5 °C) to strongly positive contributions at high temperatures (~45 °C, SHAP ≈ +10 °C). The color gradient (representing RH) reveals a humidity interaction: at temperatures above ~30 °C, points with lower RH (blue in the figure) tend to cluster at higher SHAP values than those with higher RH (pink/red). This suggests that dry heat conditions at high temperatures lead to somewhat greater T2M SHAP contributions, consistent with the VPD amplification mechanism identified in the severity-stratified analysis.

RH Dependence (Figure 10b). The RH dependence plot reveals a strongly nonlinear, monotonically decreasing relationship. At low RH values (<20%), SHAP values are strongly positive (up to +3.5 °C), while the transition to negative SHAP values occurs at approximately RH ≈ 28-30%, beyond which increasing humidity is associated with decreasing UTCI contributions. This pattern requires careful interpretation: it should not be read as direct physical evidence that higher humidity reduces heat stress. Rather, it reflects the covariance structure within the filtered dataset and the fitted model. In Türkiye's warm-season

heat-stress sample, the most extreme UTCI values often coincide with very high temperature and low-to-moderate RH in dry inland settings, whereas higher RH more commonly occurs in maritime environments where temperature is partly moderated. The color gradient confirms this: the strongest positive RH SHAP values occur at high temperatures (red/pink points at low RH), while the most negative values occur at low temperatures (blue points at high RH). The RH dependence therefore captures the conditional statistical association between moisture regime and thermal stress within this domain, not a universal physical relationship.

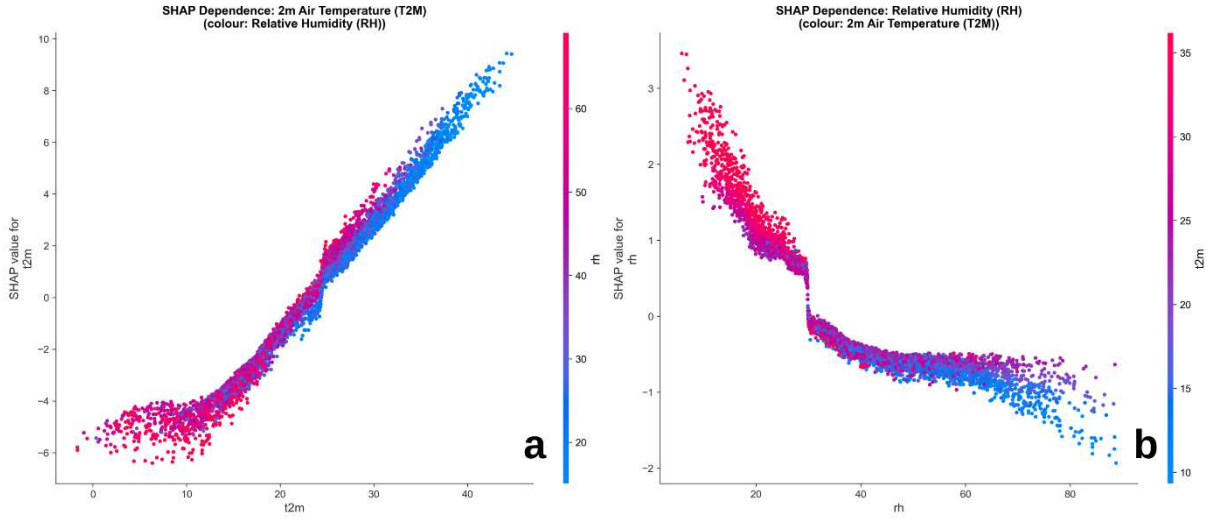


Figure 10. SHAP dependence plots showing model-attributed contributions of individual climate drivers to predicted UTCI. (a) T2M SHAP values versus air temperature, colored by Relative Humidity. (b) RH SHAP values versus Relative Humidity, colored by 2-meter Air Temperature.

4. Discussion

4.1. Principal Findings and Scientific Contribution

The main contribution of this study is not that heat stress is intensifying in the Eastern Mediterranean, since that broad conclusion is already well established in the regional literature (Lelieveld et al., 2016; Zittis et al., 2022a). Nor does the primary contribution lie in the high predictive skill of the Random Forest model, which is partly expected because UTCI is itself derived from meteorological inputs that conceptually overlap with the predictor set. Rather, the scientific value of this work resides in the systematic decomposition of thermal stress variability into spatially differentiated and severity-aware driver structures using explainable AI.

By integrating SHAP analysis at global, regional, severity-stratified, and pixel-wise scales, we have decomposed the model-attributed effects of radiation, moisture, wind, and temperature on predicted UTCI, revealing patterns that are not accessible through conventional correlation or regression approaches. To our knowledge, this represents the first study to apply XAI to systematically decompose UTCI driver importance across thermal stress severity categories at the regional climatological scale, thereby addressing a gap at the intersection of UTCI-based bioclimatology, explainable AI methodology, and severity-stratified thermal stress analysis. The novelty lies less in the prediction of a derived thermal index per se than in the spatially explicit and severity-aware attribution framework used to identify where different classes of meteorological controls become more or less prominent. The central finding is that thermal comfort drivers are neither spatially uniform nor severity-invariant. The pixel-wise SHAP map (Figure 8) provides the most compelling evidence: the dominant secondary climate driver shifts across Türkiye's climatic gradient, with VPD governing much of the semi-arid interior (~60-65% of land area), wind speed becoming comparatively more influential along the northern maritime periphery, and thermal radiation dominating discrete segments of the southern coastline. These spatial patterns are too coherent to dismiss as statistical noise; they align with the underlying thermophysiological mechanisms by which the human body exchanges heat with its environment under different atmospheric regimes. This insight is essential if heat-risk assessment is to move beyond trend description toward process-aware and region-specific adaptation planning.

4.2. Mechanistic Interpretation of Spatial Driver Patterns

The spatial coherence of the VPD-dominated interior can be interpreted through the lens of human heat balance physiology. A critical distinction must be drawn: high VPD does not indicate "humid heat" but rather atmospheric dryness and high evaporative demand. In semi-arid environments where air temperatures frequently exceed skin temperature (~35 °C), dry-bulb convective heat exchange transitions from a cooling mechanism to a heating mechanism, and the body becomes almost entirely dependent on evaporative cooling (sweat evaporation) for thermoregulation (Parsons, 2007). The rate of sweat evaporation is directly proportional to VPD: higher VPD accelerates evaporation, but the extremely high VPD values observed in Central, Eastern, and Southeastern Anatolia (often exceeding 3-4 kPa) indicate conditions where, despite high evaporative demand, the rate of metabolic heat production may exceed the rate of dissipation under extreme conditions. This finding is consistent with recent work demonstrating rising VPD as a fundamental constraint on biological evaporative cooling

(Yuan et al., 2019) and the empirical evidence that dry heat stress thresholds are substantially lower than humid heat thresholds (Vecellio et al., 2022). The conflation of humidity's role in hot-humid coastal stress with VPD's role in dry inland stress should be carefully avoided; they are related through moisture physics but not interchangeable.

The wind-dominated regime along the Black Sea coast and Marmara region reflects a fundamentally different thermodynamic pathway. In humid oceanic environments (RH typically 60-80%), evaporative cooling is inherently limited by the low VPD, and the body relies more heavily on convective heat loss via wind-driven sensible heat exchange for thermal regulation. The SHAP decomposition recovered a pattern that is consistent with established thermophysiological expectations for humid maritime environments, lending physical plausibility to the attribution results. This is consistent with the findings of Foster et al. (2022), who demonstrated that wind's cooling effectiveness depends critically on the temperature-humidity regime, and with Van der Hoeven and Wandl (2015), who found that intra-urban thermal comfort variability is mainly wind-driven during daytime.

The radiation-dominated clusters along the Mediterranean coast are consistent with the localized nature of longwave radiative heat gain from sun-heated surfaces. In the Mediterranean climate, clear skies, high solar angles, and low-albedo terrain (exposed limestone, dark soils) create intense longwave emission from the ground surface that significantly increases the mean radiant temperature, which is a key UTCI input. The patchy spatial distribution of STRD-dominant pixels suggests that terrain-scale factors such as aspect, surface material, and urbanization modulate this effect at sub-regional scales, consistent with previous observations that surface properties exert strong local control on the thermal radiation environment in Mediterranean settings (Altunkasa and Uslu, 2020).

4.3. Severity-Dependent Driver Transitions

The severity-stratified analysis provides critical insights for public health risk assessment. The finding that VPD and STRD importance escalates sharply as conditions transition from moderate to very strong heat stress (Figure 5) carries important implications: the atmospheric conditions associated with extreme physiological danger are qualitatively different from those producing moderate discomfort. The correct scientific inference is not a "humidity takeover" of temperature dominance, but rather a transition toward a more compound structure of severe heat in which atmospheric desiccation and radiative loading become increasingly consequential while temperature retains its primary role.

Specifically, during moderate heat stress (26-32 °C UTCI), the climate driver portfolio is relatively balanced, with wind speed contributing substantially (mean |SHAP| = 0.313 °C) alongside T2M and VPD. This suggests that passive cooling strategies (ventilation, air movement) remain effective mitigation measures at this severity level. At very strong heat stress (38-46 °C UTCI), VPD and STRD importance surges while wind speed collapses to 0.067 °C, a 79% reduction from moderate heat, reaching 0.019 °C at extreme heat (94% reduction). This model-attributed decline in wind importance is consistent with the experimental demonstration by Bröde and Kampmann (2023) that wind cooling reverses to heating when air temperature exceeds approximately 35 °C. At these severities, adaptation strategies must shift from ventilation-based approaches toward targeting the moisture balance (misting, humidification) and radiative environment (shading, surface albedo modification).

This severity-dependent transition has direct implications for heat action plans and early warning systems. Many existing European heat warning systems rely on temperature thresholds alone (Casanueva et al., 2019; Di Napoli et al., 2019); the present findings suggest that incorporating VPD and radiation parameters could improve risk stratification, particularly for regions where these drivers gain importance at severe heat stress levels. Heat action plans should also explicitly address the misconception that ventilation universally mitigates heat stress, particularly during extreme events where air temperature exceeds skin temperature.

4.4. Implications for Climate Adaptation

The spatially resolved driver analysis provides guidance for regionally differentiated climate adaptation strategies, a priority in the Eastern Mediterranean where adaptation planning is urgent (Ali et al., 2022; Nastos and Saaroni, 2024; Pietrapertosa et al., 2023). In the semi-arid interior (Central, Eastern, and Southeastern Anatolia), priority interventions may need to address atmospheric dryness and evaporative stress in addition to temperature exposure itself, including green infrastructure that enhances local evapotranspiration and urban design that minimizes exposure to intense dry heat. The strong VPD signal suggests that shading alone may not fully address the thermal burden in these environments. Along the northern maritime periphery (Black Sea and Marmara), maintaining or enhancing urban ventilation pathways appears particularly important: urban planning should preserve and enhance wind corridors, building orientation should maximize exposure to prevailing maritime winds, and coastal vegetation management should avoid creating wind barriers; the strong wind dependence also suggests that calm-wind periods represent disproportionate heat risk events in these regions. Along the southern coastline (Mediterranean and Aegean), radiative shading solutions such as

reflective building materials, urban tree canopies, shade structures, and cool-surface technologies (Santamouris, 2014) appear especially relevant for reducing radiative heat load. The dominance of STRD suggests that lowering mean radiant temperature through urban design interventions may provide comparatively large thermal comfort benefits in these settings, consistent with the documented effectiveness of combined nature-based solutions in Mediterranean climates (Bouketta et al., 2024; Cascone and Leuzzo, 2023).

4.5. Temporal Trends and Future Projections

The 75-year temporal analysis (Figure 2) demonstrates that the spatial driver patterns documented in this study are set against a backdrop of intensifying heat stress. The statistically significant acceleration of very strong heat events (Mann-Kendall $\tau = 0.336$, $p < 0.001$; +4.5 grid-days/year) implies that the conditions under which VPD and STRD become the dominant drivers (i.e., the upper tail of the heat stress distribution) will become increasingly frequent. The extreme heat trend (+0.8 grid-days/year), while not statistically significant at the 0.05 level ($p = 0.092$), shows a visually consistent upward drift that may reflect the rarity and high interannual variability of events in this tail category rather than the absence of a physical trend. The nonlinear nature of the severity-dependent driver transition (Section 3.4) suggests a potential regime shift: as mean temperatures rise, a disproportionately large number of previously moderate-stress days will cross into the very strong and extreme stress categories where fundamentally different atmospheric mechanisms dominate. This has cascading implications for the effectiveness of current heat mitigation infrastructure, much of which was designed for moderate heat conditions. These temporal patterns are consistent with the centennial-scale analyses of Founda et al. (2022) in Athens and the UTCI trend intensification documented by Katavoutas and Founda (2019), who observed the "very strong heat stress" season elongating by approximately 4.3 days per decade over the past six decades.

4.6. Methodological Considerations

The approach of computing SHAP values for every individual grid cell, rather than aggregating at the regional level, represents a methodological contribution that extends beyond the specific findings reported here. This pixel-wise SHAP mapping technique reveals intra-regional heterogeneity, such as the sharp VPD-to-wind transition at the Pontic Mountain crest, that is invisible in regional aggregations and enables climate adaptation strategies to be tailored at sub-regional scales. Similar spatial SHAP mapping approaches have been demonstrated for susceptibility modeling (Wang et al., 2024) and urban thermal comfort

prediction (Zhang et al., 2025), suggesting a broader applicability of this methodology across geoscience applications.

4.7. Limitations

Several limitations should be acknowledged. First, the study relies on reanalysis data, and ERA5, while representing the current state of the art (Hersbach et al., 2020), may underrepresent localized phenomena such as urban heat islands, foehn winds, and micro-scale topographic effects that influence thermal comfort at the neighborhood scale. The 0.25° spatial resolution (~25 km) is coarse relative to urban morphology, and ERA5-HEAT UTCI has been reported to exhibit an RMSE of approximately 5.2 ± 2.5 °C against station observations (Di Napoli et al., 2021), though recent evaluations suggest it performs well as a proxy for field measurements (Krüger and Di Napoli, 2022). The results should therefore be interpreted at the synoptic-to-regional scale.

Second, UTCI is derived from meteorological variables that overlap conceptually with the predictor set (air temperature, humidity, wind, radiation). This means the model is not discovering an entirely external relationship; it is reorganizing information from a related meteorological space. The high predictive skill ($R^2 = 0.936$) is therefore partly structural, and the scientific contribution lies in the attribution structure, specifically in identifying which variables matter most, where, and under what conditions, rather than in prediction per se. Accordingly, the present framework should be interpreted as an attribution-oriented decomposition of a derived thermal index within meteorologically related predictor space, not as an attempt to predict an unrelated target variable.

Third, the predictor variables are limited to seven climate drivers from ERA5-Land. Important factors such as mean radiant temperature (computed internally in UTCI but not used as an explicit predictor), urban geometry, land cover type, and anthropogenic heat emissions are not represented, though their effects may be partially captured through the radiation and temperature variables. Relatedly, RH, VPD, and Q are partially overlapping representations of atmospheric moisture. Their SHAP rankings may therefore reflect attribution sharing within a correlated predictor space, and should not be interpreted as fully independent physical effect estimates.

Fourth, while RF models effectively capture nonlinear relationships, they may underperform compared to gradient boosting methods (XGBoost; Chen and Guestrin, 2016) for certain interaction patterns. Recent comparisons in the thermal comfort domain show mixed results

(Guo et al., 2024; Karimi et al., 2025), and future work should compare multiple ML architectures.

Fifth, the severity-stratified and pixel-wise analyses are based on time-averaged conditions and do not capture temporal dynamics such as heat wave evolution, diurnal cycling, or synoptic-scale weather pattern effects on driver importance. The use of daily aggregated predictors may smooth sub-daily controls that are important for UTCI maxima, particularly radiation and wind speed at the hour when maximum UTCI occurs. The predictors therefore characterize event-day thermal environments rather than the exact instantaneous meteorological state associated with the UTCI peak.

Sixth, SHAP values explain the fitted model rather than establishing physical causality in a strict experimental sense. The language throughout this manuscript therefore refers to model-attributed importance rather than definitive physical mechanisms. When interpreting SHAP results, it is essential to recognize that correlated predictors share attribution in ways that may not correspond to independent physical pathways.

Seventh, the trend analysis shown in Figure 2 was formally evaluated using Mann–Kendall tests. The very strong heat series exhibited a statistically significant increasing trend, whereas the extreme heat series showed a positive but weaker trend that did not reach conventional significance levels. The remaining limitation is therefore not the absence of trend testing, but the fact that the analysis was restricted to monotonic trend detection and did not evaluate more complex temporal structures such as step changes, nonlinearity, or changing variance.

Eighth, the current train/test split uses random sampling, which may produce somewhat optimistic skill estimates because spatially and temporally adjacent grid-day observations are not fully independent. The reported performance metrics should therefore be interpreted primarily as evidence of internal model stability for attribution analysis rather than as strict measures of fully independent predictive generalization. Future work should evaluate model robustness using spatially blocked or temporally blocked cross-validation.

In addition, RH, VPD, and Q represent partially overlapping thermodynamic descriptions of atmospheric moisture. Their SHAP rankings should therefore be interpreted as relative attributions within a correlated moisture space, rather than as fully independent physical pathways.

5. Conclusions

This study presents a comprehensive, multi-scale explainable machine learning framework for decoding the spatial and severity-dependent dynamics of thermal comfort across Türkiye, an Eastern Mediterranean climate change hotspot. The principal conclusions are:

1. A Random Forest Regressor achieves $R^2 = 0.936$ for predicting daily maximum UTCI from seven climate variables across 826,799 grid-day observations spanning 75 years (1950-2025), indicating that the selected predictor set provides a sufficiently stable basis for attribution-focused XAI analysis of daily maximum UTCI.

2. The severity-stratified SHAP analysis reveals a critical nonlinear transition: as heat stress intensifies from moderate (26-32 °C) to very strong (38-46 °C), VPD importance increases by 66% and STRD importance doubles, while wind speed importance collapses by 94%. This pattern suggests that severe thermal stress is associated with a markedly different balance of model-attributed meteorological controls than moderate discomfort.

3. The pixel-wise (0.25° × 0.25°) SHAP map reveals three distinct spatial regimes of secondary driver dominance: VPD across the semi-arid interior (~60-65% of land area), wind speed along the northern maritime coast, and thermal radiation along the southern coastline, with these patterns being broadly consistent with known thermophysiological heat-exchange pathways under contrasting climatic settings.

4. Very strong heat (38-46 °C UTCI) events have increased at +4.5 grid-days/year and extreme heat (>46 °C) events at +0.8 grid-days/year over 1950-2025, implying that the severe-heat driver regimes will become increasingly prevalent under continued warming.

5. Effective heat mitigation requires fundamentally different strategies across regions: combating atmospheric desiccation in the interior, enhancing ventilation infrastructure along the northern coasts, and deploying radiative shading solutions along the southern Mediterranean coastline.

These findings provide a data-driven, spatially resolved foundation for climate adaptation planning in the Eastern Mediterranean and demonstrate the potential of XAI methodologies for extracting mechanistic insights from complex environmental datasets.

Author Contributions

[To be completed]

Funding

[To be completed]

Data Availability

ERA5 and ERA5-HEAT data are publicly available through the Copernicus Climate Data Store (https://cds.climate.copernicus.eu/). The boundary data for Türkiye's geographic regions were obtained from official geographic databases. All analysis code is available upon request.

Declaration of Competing Interests

The authors declare no competing interests.

References

Ahmadalipour A, Moradkhani H (2018) Escalating heat-stress mortality risk due to global warming in the Middle East and North Africa (MENA). Environ Int 117:215-225. https://doi.org/10.1016/j.envint.2018.05.014

Ali E, Cramer W, Carnicer J, Georgopoulou E, Hilmi NJM, Le Cozannet G, Lionello P (2022) Cross-Chapter Paper 4: Mediterranean Region. In: Pörtner HO, Roberts DC, Tignor M, et al (eds) Climate Change 2022: Impacts, Adaptation and Vulnerability. Contribution of Working Group II to the Sixth Assessment Report of the Intergovernmental Panel on Climate Change. Cambridge University Press, Cambridge, UK and New York, NY, USA, pp 2233–2272. https://doi.org/10.1017/9781009325844.021

Allen RG, Pereira LS, Raes D, Smith M (1998) Crop evapotranspiration: Guidelines for computing crop water requirements. FAO Irrigation and Drainage Paper No. 56. Food and Agriculture Organization of the United Nations, Rome, Italy

Altunkasa MF, Uslu C (2020) Use of outdoor microclimate simulation maps for a planting design to improve thermal comfort. Sustain Cities Soc 57:102134. https://doi.org/10.1016/j.scs.2020.102134

Błażejczyk K, Epstein Y, Jendritzky G, Staiger H, Tinz B (2012) Comparison of UTCI to selected thermal indices. Int J Biometeorol 56:515-535. https://doi.org/10.1007/s00484-011-0455-5

Błażejczyk K, Jendritzky G, Bröde P, Fiala D, Havenith G, Epstein Y, Psikuta A, Kampmann B (2013) An introduction to the Universal Thermal Climate Index (UTCI). Geographia Polonica 86:5-10. https://doi.org/10.7163/GPol.2013.1

Błażejczyk K, Kuchcik M (2021) UTCI-10 years of applications. Int J Biometeorol 65:1631-1635. https://doi.org/10.1007/s00484-021-02109-3

Bommer PL, Kretschmer M, Hedström A, Bareeva D, Höhne MM-C (2024) Finding the right XAI method-A guide for the evaluation and ranking of explainable AI methods in climate science. Artif Intell Earth Syst 3:e230074. https://doi.org/10.1175/AIES-D-23-0074.1

Bouketta S, Bouchahm Y, Djekic J (2024) Coupling of different nature-based solutions for pedestrian thermal comfort in a Mediterranean climate. Build Environ 255:111413. https://doi.org/10.1016/j.buildenv.2024.111413

Breiman L (2001) Random Forests. Mach Learn 45:5-32. https://doi.org/10.1023/A:1010933404324

Briegel F, Wehrle J, Schindler D, Christen A (2024) High-resolution multi-scaling of outdoor human thermal comfort and its intra-urban variability based on machine learning. Geosci Model Dev 17:1667-1688. https://doi.org/10.5194/gmd-17-1667-2024

Bröde P, Fiala D, Błażejczyk K, Holmér I, Jendritzky G, Kampmann B, Tinz B, Havenith G (2012) Deriving the operational procedure for the Universal Thermal Climate Index (UTCI). Int J Biometeorol 56:481-494. https://doi.org/10.1007/s00484-011-0454-6

Bröde P, Kampmann B (2023) Temperature–Humidity-Dependent Wind Effects on Physiological Heat Strain of Moderately Exercising Individuals Reproduced by the Universal Thermal Climate Index (UTCI). Biology 12:802. https://doi.org/10.3390/biology12060802

Casanueva A, Burgstall A, Kotlarski S, Messeri A, Morabito M, Schwierz C, Töglhofer C (2019) Overview of existing heat-health warning systems in Europe. Int J Environ Res Public Health 16:2657. https://doi.org/10.3390/ijerph16152657

Cascone S, Leuzzo A (2023) Thermal comfort in the built environment: a digital workflow for the comparison of different green infrastructure strategies. Atmosphere 14:685. https://doi.org/10.3390/atmos14040685

Chen T, Guestrin C (2016) XGBoost: A scalable tree boosting system. In: Proceedings of the 22nd ACM SIGKDD International Conference on Knowledge Discovery and Data Mining. ACM, New York, pp 785-794. https://doi.org/10.1145/2939672.2939785

Cos J, Doblas-Reyes F, Jury M, Marcos R, Bretonnière P-A, Samsó M (2022) The Mediterranean climate change hotspot in the CMIP5 and CMIP6 projections. Earth Syst Dyn 13:321-340. https://doi.org/10.5194/esd-13-321-2022

Di Napoli C, Barnard C, Prudhomme C, Cloke HL, Pappenberger F (2021) ERA5-HEAT: A global gridded historical dataset of human thermal comfort indices from climate reanalysis. Geosci Data J 8:2-10. https://doi.org/10.1002/gdj3.137

Di Napoli C, Pappenberger F, Cloke HL (2018) Assessing heat-related health risk in Europe via the Universal Thermal Climate Index (UTCI). Int J Biometeorol 62:1155-1165. https://doi.org/10.1007/s00484-018-1518-2

Di Napoli C, Pappenberger F, Cloke HL (2019) Verification of heat stress thresholds for a health-based heat-wave definition. J Appl Meteorol Climatol 58:1177-1194. https://doi.org/10.1175/JAMC-D-18-0240.1

Fiala D, Havenith G, Bröde P, Kampmann B, Jendritzky G (2012) UTCI-Fiala multi-node model of human heat transfer and temperature regulation. Int J Biometeorol 56:429-441. https://doi.org/10.1007/s00484-011-0451-6

Flora ML, Potvin CK, McGovern A, Handler S (2024) A machine learning explainability tutorial for atmospheric sciences. Artif Intell Earth Syst 3:e230018. https://doi.org/10.1175/AIES-D-23-0018.1

Foster J, Smallcombe JW, Hodder S, Jay O, Flouris AD, Havenith G (2022) Quantifying the impact of heat on human physical work capacity; part II: the observed interaction of air velocity with temperature, humidity, sweat rate, and clothing. Int J Biometeorol 66:507-520. https://doi.org/10.1007/s00484-021-02231-2

Founda D, Katavoutas G, Pierros F, Mihalopoulos N (2022) Centennial changes in heat waves characteristics in Athens (Greece) from multiple definitions based on climatic and bioclimatic indices. Glob Planet Change 212:103807. https://doi.org/10.1016/j.gloplacha.2022.103807

Gholami H, Falah F, Azarafza M, Mohammadi P, Jafari A, Lee S, Tien Bui D (2024) An interpretable model based on machine learning and SHAP interpretation technique for mapping wind erosion hazard. Environ Sci Pollut Res 31:64628-64643. https://doi.org/10.1007/s11356-024-32450-8

Giorgi F (2006) Climate change hot-spots. Geophys Res Lett 33:L08707. https://doi.org/10.1029/2006GL025734

Guo R, Yang B, Guo Y, Li H, Li Z, Zhou B, Hong B, Wang F (2024) Machine learning-based prediction of outdoor thermal comfort: Combining Bayesian optimization and the SHAP model. Build Environ 254:111301. https://doi.org/10.1016/j.buildenv.2024.111301

Hamed MM, Nashwan MS, Shahid S (2023) Spatiotemporal changes in Universal Thermal Climate Index in the Middle East and North Africa. Atmos Res 298:107089. https://doi.org/10.1016/j.atmosres.2023.107089

Havenith G, Fiala D, Błażejczyk K, Richards M, Bröde P, Holmér I, Rintamäki H, Benshabat Y, Jendritzky G (2012) The UTCI-clothing model. Int J Biometeorol 56:461-470. https://doi.org/10.1007/s00484-011-0458-2

He Z, Yang Y, Fang R, Zhou S, Zhao W, Bai Y, Ma Y, Guan Y, Tang X, Wang B (2023) Integration of shapley additive explanations with random forest model for quantitative precipitation estimation of mesoscale convective systems. Front Environ Sci 10:1057081. https://doi.org/10.3389/fenvs.2022.1057081

Hersbach H, Bell B, Berrisford P, Biavati G, Horányi A, Muñoz Sabater J, Nicolas J, Peubey C, Radu R, Rozum I, Schepers D, Simmons A, Soci C, Dee D, Thépaut J-N (2020) The ERA5 global reanalysis. Q J R Meteorol Soc 146:1999-2049. https://doi.org/10.1002/qj.3803

Hong T, Yim SHL, Heo Y (2025) Interpreting complex relationships between urban and meteorological factors and street-level urban heat islands: Application of random forest and SHAP method. Sustain Cities Soc 120:106XXX. https://doi.org/10.1016/j.scs.2025.106XXX

Jendritzky G, de Dear R, Havenith G (2012) UTCI-Why another thermal index? Int J Biometeorol 56:421-428. https://doi.org/10.1007/s00484-011-0455-4

Jiang Z, Bevacqua E, Zscheischler J (2024) How interpretable machine learning can benefit process understanding in the geosciences. Earths Future 12:e2024EF004540. https://doi.org/10.1029/2024EF004540

Karimi S, Khodakarami J, Rotuno Tinti F, Golibaghghi M, Carmeliet J (2025) A measurement-based framework integrating machine learning and morphological dynamics for outdoor thermal regulation. Int J Biometeorol. https://doi.org/10.1007/s00484-024-02711-6

Katavoutas G, Founda D (2019) Intensification of thermal risk in Mediterranean climates: Evidence from the comparison of rational and simple indices. Int J Biometeorol 63:1251-1264. https://doi.org/10.1007/s00484-019-01724-4

Kim J, Zhou Y, Schiavon S, Raftery P, Brager G (2018) Personal comfort models: Predicting individuals' thermal preference using occupant heating and cooling behavior and machine learning. Build Environ 129:96-106. https://doi.org/10.1016/j.buildenv.2017.12.024

Krüger EL, Di Napoli C (2022) Feasibility of climate reanalysis data as a proxy for onsite weather measurements in outdoor thermal comfort surveys. Theor Appl Climatol 149:1645-1658. https://doi.org/10.1007/s00704-022-04123-4

Kuglitsch FG, Toreti A, Xoplaki E, Della-Marta PM, Zerefos CS, Türkeş M, Luterbacher J (2010) Heat wave changes in the eastern Mediterranean since 1960. Geophys Res Lett 37:L04802. https://doi.org/10.1029/2009GL041888

Lelieveld J, Hadjinicolaou P, Kostopoulou E, Chenoweth J, El Maayar M, Giannakopoulos C, Hannides C, Lange MA, Tanarhte M, Tyrlis E, Xoplaki E (2012) Climate change and impacts in the Eastern Mediterranean and the Middle East. Clim Change 114:667-687. https://doi.org/10.1007/s10584-012-0418-4

Lelieveld J, Proestos Y, Hadjinicolaou P, Tanarhte M, Tyrlis E, Zittis G (2016) Strongly increasing heat extremes in the Middle East and North Africa (MENA) in the 21st century. Clim Change 137:245-260. https://doi.org/10.1007/s10584-016-1665-6

Lionello P, Scarascia L (2018) The relation between climate change in the Mediterranean region and global warming. Reg Environ Change 18:1481-1493. https://doi.org/10.1007/s10113-018-1290-1

Lundberg SM, Erion G, Chen H, DeGrave A, Prutkin JM, Nair B, Katz R, Himmelfarb J, Bansal N, Lee SI (2020) From local explanations to global understanding with explainable AI for trees. Nat Mach Intell 2:56-67. https://doi.org/10.1038/s42256-019-0138-9

Lundberg SM, Lee SI (2017) A unified approach to interpreting model predictions. Adv Neural Inf Process Syst 30:4765-4774. https://doi.org/10.48550/arXiv.1705.07874

Mora C, Dousset B, Caldwell IR, Powell FE, Geronimo RC, Bielber CR, Counsell BW, Dietrich BS, Johnston EW, Louis LV, Lucas MP, McKenzie MM, Shea AG, Tseng H, Giambelluca TW, Leon LR, Hawkins E, Trauernicht C (2017) Global risk of deadly heat. Nat Clim Change 7:501-506. https://doi.org/10.1038/nclimate3322

Nastos P, Saaroni H (2024) Living in Mediterranean cities in the context of climate change: A review. Int J Climatol 44:3169-3190. https://doi.org/10.1002/joc.8169

Nazarian N, Krayenhoff ES, Bechtel B, Hondula DM, Paolini R, Vanos J, Vantrepotte V, Middel A, Talaei S, Cheung T, Foster J, Lee JKW, Chow WTL (2022) Integrated assessment of urban overheating impacts on human life. Earths Future 10:e2022EF002682. https://doi.org/10.1029/2022EF002682

Ntoumos A, Hadjinicolaou P, Zittis G, Lelieveld J (2022) Projected Air Temperature Extremes and Maximum Heat Conditions Over the MENA Region. Earth Syst Environ 6:343-356. https://doi.org/10.1007/s41748-022-00246-2

Özturk T, Ceber ZP, Türkeş M, Kurnaz ML (2015) Projections of climate change in the Mediterranean Basin by using downscaled global climate model outputs. Int J Climatol 35:4276-4292. https://doi.org/10.1002/joc.4285

Pappenberger F, Jendritzky G, Staiger H, Dutra E, Di Giuseppe F, Richardson DS, Cloke HL (2015) Global forecasting of thermal health hazards. Int J Biometeorol 59:311-323. https://doi.org/10.1007/s00484-014-0843-3

Parsons K (2007) Human Thermal Environments: The Effects of Hot, Moderate, and Cold Environments on Human Health, Comfort, and Performance, 3rd edn. CRC Press, Boca Raton

Pietrapertosa F, Olazabal M, Simões SG, Salvia M, Fokaides PA, Kyriakopoulos G, Spyridaki N, Zaganczyk K, Kurnik B, Swiderska M, Ruggiero S, Di Munno R, Manfren M, De Felice M, Musco A, Damm A, Vollmer D, Schaub S, Smigaj M, Magdziak M, Tikkanen J, Marin J, Sanz MJ, Lo Presti V, Fonti V, Gagliano A, Gori A, Pacheco MM, Sousedik B, Berry PM (2023) Adaptation to climate change in cities of Mediterranean Europe. Cities 140:104459. https://doi.org/10.1016/j.cities.2023.104459

Potchter O, Cohen P, Lin TP, Matzarakis A (2018) Outdoor human thermal perception in various climates: A comprehensive review of approaches, methods and quantification. Sci Total Environ 631:390-406. https://doi.org/10.1016/j.scitotenv.2018.03.184

Provençal S, Bergeron O, Leduc R, Barrette N (2016) Thermal comfort in Quebec City, Canada: sensitivity analysis of the UTCI and other popular thermal comfort indices in a mid-latitude continental city. Int J Biometeorol 60:591-603. https://doi.org/10.1007/s00484-015-1066-8

Raymond C, Matthews T, Horton RM (2020) The emergence of heat and humidity too severe for human tolerance. Sci Adv 6:eaaw1838. https://doi.org/10.1126/sciadv.aaw1838

Reichstein M, Camps-Valls G, Stevens B, Jung M, Denzler J, Carvalhais N, Prabhat (2019) Deep learning and process understanding for data-driven Earth system science. Nature 566:195-204. https://doi.org/10.1038/s41586-019-0912-1

Santamouris M (2014) Cooling the cities-a review of reflective and green roof mitigation technologies. Sol Energy 103:682-703. https://doi.org/10.1016/j.solener.2013.12.006

Sherwood SC, Huber M (2010) An adaptability limit to climate change due to heat stress. Proc Natl Acad Sci 107:9552-9555. https://doi.org/10.1073/pnas.0913352107

Simpson CH, Brousse O, Ebi KL, Heaviside C (2023) Commonly used indices disagree about the effect of moisture on heat stress. npj Clim Atmos Sci 6:78. https://doi.org/10.1038/s41612-023-00408-x

Soci C, Hersbach H, Simmons A, Berrisford P, Poli P, Dee D, Peubey C, Radu R, Rayner N, Oki T (2024) The ERA5 global reanalysis from 1940 to 2022. Q J R Meteorol Soc 150. https://doi.org/10.1002/qj.4803

Taşoğlu E, Öztürk MZ, Yazıcı Ö (2024) High Resolution Köppen-Geiger Climate Zones of Türkiye. Int J Climatol 44:5248-5265. https://doi.org/10.1002/joc.8635

Urban A, Di Napoli C, Cloke HL, Kyselý J, Pappenberger F, Sera F, Gasparrini A (2021) Evaluation of the ERA5 reanalysis-based Universal Thermal Climate Index on mortality data in Europe. Environ Res 198:111227. https://doi.org/10.1016/j.envres.2021.111227

Van der Hoeven F, Wandl A (2015) Temporal and spatial variability of urban heat island and thermal comfort within the Rotterdam agglomeration. Build Environ 83:91-103. https://doi.org/10.1016/j.buildenv.2014.05.015

Vecellio DJ, Kong Q, Kenney WL, Huber M (2023) Greatly enhanced risk to humans as a consequence of empirically determined lower moist heat stress tolerance. Proc Natl Acad Sci 120:e2305427120. https://doi.org/10.1073/pnas.2305427120

Vecellio DJ, Wolf ST, Cottle RM, Kenney WL (2022) Evaluating the 35 °C wet-bulb temperature adaptability threshold for young, healthy subjects (PSU HEAT Project). J Appl Physiol 132:340-345. https://doi.org/10.1152/japplphysiol.00790.2021

Wang N, Zhang H, Dahal A, Cheng W, Zhao M, Lombardo L (2024) On the use of explainable AI for susceptibility modeling: Examining the spatial pattern of SHAP values. Geosci Front 15:101800. https://doi.org/10.1016/j.gsf.2024.101800

Yılmaz M, Kara Y, Toros H, İncecik S (2024) Analysis of the summer thermal comfort indices in İstanbul. Int J Biometeorol 68:1327-1342. https://doi.org/10.1007/s00484-024-02633-3

Yuan W, Zheng Y, Piao S, Ciais P, Lombardozzi D, Wang Y, Ryu Y, Chen G, Dong W, Hu Z, Jain AK, Jiang C, Kato E, Li S, Lienert S, Liu S, Nabel JEMS, Qin Z, Quine T, Sitch S, Smith WK, Wang F, Wu C, Xiao Z, Yang S (2019) Increased atmospheric vapor pressure deficit reduces global vegetation growth. Sci Adv 5:eaax1396. https://doi.org/10.1126/sciadv.aax1396

Zhang X, Chen T, Zhang S, Yuan C, Tan PY (2025) Toward healthy neighborhood thermal environments: Interpretation of thermal comfort and rapid identification of hotspot areas using image-based metrics and explainable machine learning. Sustain Cities Soc 120:106648. https://doi.org/10.1016/j.scs.2024.106648

Zittis G, Almazroui M, Alpert P, Ciais P, Cramer W, Dahdal Y, Fnais M, Francis D, Hadjinicolaou P, Howari F, Jrrar A, Klingmüller K, Lelieveld J, Lelieveld J, Lionello P, Losic L, Luterbacher J, Manzanas R, Mariotti A, Michaelides S, Pal JS, Perkins-Kirkpatrick SE, Scoccimarro E, Solmon F, Torma C, Ztitis G (2022) Climate Change and Weather Extremes in the Eastern Mediterranean and Middle East. Rev Geophys 60:e2021RG000762. https://doi.org/10.1029/2021RG000762

Zittis G, Hadjinicolaou P, Fnais M, Lelieveld J (2016) Projected changes in heat wave characteristics in the eastern Mediterranean and the Middle East. Reg Environ Change 16:1863-1876. https://doi.org/10.1007/s10113-016-0995-3

Statements & Declarations

Funding

Not applicable. The authors received no specific funding for this study.

Competing Interests

The authors have no relevant financial or non-financial interests to disclose.

Availability of data and material

The ERA5-Land reanalysis dataset used in this study is publicly available from the Copernicus Climate Change Service (C3S). Any additional processed data or materials that support the findings of this study are available from the corresponding author upon reasonable request.

Code availability

The Python scripts used for data analysis and figure preparation are available from the corresponding author upon reasonable request.

Authors' contributions

D.D.Y. conceived and designed the study, conducted all analyses, prepared all figures and tables, wrote the manuscript, and reviewed and approved the final version.